https://doi.org/10.52131/jmps.2020.0102.0007

Journal of Materials and Physical Sciences

Volume 1, Number 2, 2020, Pages 58 - 77

Journal Homepage:
https://journals.internationalrasd.org/index.php/jmps

Doping Effect and Microstructure Behavior of Rare-Earth Element Cerium (Ce^{+3}) in Barium Hexaferrite ($BaCe_xFe_{12-x}O_{19}$) Nanoparticles

Zaheer Abbas Gilani[1], Awais Ahmed[1], H. M. Noor ul Huda Khan Asghar[1*], Muhammad Khalid[2]

[1] Department of Physics, Balochistan University of Information Technology, Engineering & Management Sciences, Quetta 87300, Pakistan
[2] Department of Physics, University of Karachi 24700, Pakistan

ARTICLE INFO

Article History:
Received: September 07, 2020
Revised: October 30, 2020
Accepted: November 29, 2020
Available Online: December 31, 2020

Keywords:
Hexaferrites
Sol-gel
XRD
Rietveld
Crystalline Size
FTIR
Dielectric Analysis

ABSTRACT

Cerium substituted BaM hexaferrites $BaCe_xFe_{12-x}O_{19}$ (x = 0.0, 0.25, 0.5, 0.75, and 1.0) nano crystallites were synthesized via Sol-gel method. The x-ray diffraction (XRD) patterns were analyzed by Rietveld refinement which confirms the formation of hexagonal structure. The crystalline size was calculated by Debye Scherrer method, W–H method and SSP method. The lattice constant α found to decrease, this was due to the octahedral site replacing a large radius of Ce^{3+} ion with a smaller radius Fe^{3+} ion, While the lattice constant c found increase. The x-ray density observed increases with increasing Ce^{3+} concentration. Fourier transform infrared spectroscopy (FTIR) confirmed the two frequency bands υ_1 tetrahedral site and υ_2 octahedral site in a range between 400–620 cm^{-1}. Impedance analyzer was used to investigate the dielectric properties in a range of 1 MHz – 3 GHz following Maxwell Wagner model. Dielectric constant showed decreasing trend while dielectric loss showed dispersive behavior by increasing frequency and same was that with tangent loss, such behavior was due to Koop's phenomenological theory. AC conductivity exhibits a plane behavior in a low frequency, while dispersive in high frequency. Such behavior was due to grain effect at high frequency. Impedance showed continuous action at high frequency, which is attributed to the release of space charges. The real and imaginary modulus showed variation by increasing frequency, which was due to the occurrence of relaxation phenomenon. As per dielectric research, these ferrites can be utilized in high frequency devices, microwave technologies, and semiconductor devices.

*Corresponding Author's Email: noorulhudakhan@gmail.com

1. Introduction

Nanotechnology research is becoming one of the most important and rapidly expanding fields. Nano-sized ferrites, in particular, are being studied to improve their structural and electrical properties in order to make them suitable for high frequency applications and other advanced electronic devices (N. Singh, Agarwal, Sanghi, & Singh, 2011). Last few years, scientists are showing interest in hexagonal ferrites. There are different types of hexagonal ferrites which are also famous as hexaferrites have their long journey since their discovery, (Jasrotia, Singh, Sharma, Kumar, & Singh, 2019; Jasrotia, Singh, Sharma, & Singh, 2019) one of them is M-type ferrites, Barium ferrite or BaM ($BaFe_{12}O_{19}$). Hexagonal M-type barium ferrite ($BaFe_{12}O_{19}$) and its doping element cerium (Ce^{+3}) have attracted a lot of interest due to its technological uses in permanent magnets

and prospective applications in high density magnetic recording media and microwave devices, big crystalline anisotropy, large magnetism, strong intrinsic coercivity, great chemical stability, high Curie temperature, and cheap cost characterize barium hexaferrites (Hussain et al., 2011; Iqbal, Ashiq, Hernández-Gómez, Muñoz, & Cabrera, 2010; Martirosyan, Galstyan, Hossain, Wang, & Litvinov, 2011). Due to their outstanding magnetic and dielectric characteristics, hexaferrites might be regarded one of the finest magnetic materials for electromagnetic wave absorbers (C.-J. Li, Wang, & Wang, 2012).

Barium hexaferrite has been extensively investigated as one of the most significant microwave absorption materials due to its outstanding magnetic and microwave characteristics (Choopani, Keyhan, Ghasemi, Sharbati, & Alam, 2009; L. Li et al., 2013). Generally, resistivity of barium ferrite is very high so, the dominant absorbing mechanism is magnetic loss (P. Singh et al., 2006). Hence, an improvement in the intrinsic magnetic properties such as saturation magnetization and magneto crystalline anisotropy or coercivity can enhance their microwave absorbing ability. One of the most essential instruments for satisfying a wide range of uses is doping some suitable elements in the parent material. The structural and electromagnetic behavior of ferrites are tailored by the synthetic methods and doping of various rare earth/transition metal ions in hexagonal structure (Al-Hilli, Li, & Kassim, 2009). The intrinsic properties of ferrites like permittivity, dielectric losses and conductivity are controlled by chemical composition, annealing treatment and type of doped metal ions (Al-Hilli, Li, & Kassim, 2012; Jing, Liangchao, & Feng, 2007). Magnetic and dielectric properties can be improved by elemental substitutions to ferric (Fe^{+3}) sites.

Researchers reported, when cerium (Ce^{+3}) is doped in barium hexaferrite, the microwave absorbing ability is considerably enhanced, suggesting that ($BaCe_xFe_{12-x}O_{19}$) can be utilized in microwave technology, high storage devices, and electronic components (Chang, Kangning, & Pengfei, 2012). the present study, the barium hexaferrite ($BaCe_xFe_{12-x}O_{19}$) having cerium (Ce^{+3}) as a substituent are prepared via solgel method. In this work, the doping effect and microstructure behavior of cerium (Ce^{+3}) in barium hexaferrite with general formula $BaCe_xFe_{12-x}O_{19}$ (x = 0.0, 0.25, 0.5, 0.75, 1.0) has been investigated. The prepared ferrite material is characterized by x-ray diffraction (XRD), Fourier transform infrared spectroscopy (FTIR) and dielectric properties analysis.

2. Experimental

The cerium (Ce^{+3}) substituted barium hexaferrite ($BaCe_xFe_{12-x}O_{19}$) nanoparticles were effectively produced through different cerium (Ce^{+3}) concentrations (x = 0.0, 0.25, 0.5, 0.75, and 1.0) using solgel method. The materials used were comprise of barium nitrate [Ba $(NO_3)_2$ (M.W = 261.34)] with molarity of 0.1, cerium nitrate [Ce $(NO_3)_3$ (M.W = 434.22)] with molarity of 0.1, ferric nitrate [Fe $(NO_3)_3.9H_2O$ (M.W = 404)] with molarity of 1.2, and citric acid [$C_6H_8O_7.H_2O$ (M.W = 210.14)] with molarity of 1.3, stayed systematically through physical balance. The distilled water was used for the sample preparation. All the mixtures were kept on the hot plate magnetic stirrer at 80°C for 3 hours. The evaporation was done in the thermostat oven at 90°C. After grinding, the samples were annealed at 900°C for 3 hours in box-type resistance furnace.

The x-ray diffraction (XRD) was carried out on (PANalytical X'Pert Pro) by Rietveld refinement process to analyze the crystal structure and to find various structural parameters of materials pertaining to the crystalline structure. The crystalline size of the prepared samples was confirmed by x-ray diffraction (XRD) measurements via Debye Scherrer formula. The 2θ = 32° extremely intense peaks of (107) *hkl* formed, which were an ideal peak for hexaferrite nanoparticles. The crystalline size was also investigated by W-H method and SSP method. The Fourier transform infrared spectroscopy (FTIR) analysis was done and investigated the two frequency bands which were ν_1 and ν_2 in the range of 400 – 500cm^{-1} and 500 – 620cm^{-1}. These two investigated bands were associated with tetrahedral and octahedral starching bands. The dielectric analysis was used to investigate the dielectric properties of prepared material. Various dielectric parameters like dielectric constant, dielectric loss, tangent loss, alternation current (AC) conductivity, real and imaginary part of impedance and modulus were calculated in the frequency range of 1 MHz – 3 GHz.

3. Results and Discussion

3.1. XRD Analysis

The cerium (Ce^{+3}) doped barium hexaferrites formed by solgel method are seen in the common configuration of materials with $BaCe_xFe_{12-x}O_{19}$ (x = 0.0, 0.25, 0.5, 0.75, and 1.0). To ensure that the crystal shape and size the (Panalytical X'pert Pro) is used for x-ray diffraction (XRD) characterization. This is a very useful and important characterization procedure that determines various structural parameters of materials of various compositions, such as lattice constant, crystallite size, unit cell length, x-ray density and bulk density, dislocation density, stacking fault, lattice strain and micro strain, and cell volume. The crystalline stage of the prepared samples is confirmed by x-ray diffraction (XRD) measurements. The most intense peaks of all the samples are observed at angle 2θ = 32° having (107) *hkl* miller indices, which are ideal peaks for hexagonal structure. (Lodhi et al., 2014) No impurity phase is detected in XRD analysis. The peaks corresponding to x-ray diffraction (XRD) pattern are studied and are indexed as (006), (107), (205), (1011), (218), and (2014), which confirms the hexagonal structure. These peaks are verified by JCPDS card number 00-027-1029. In (Figure 1), the XRD pattern of the prepared samples $BaCe_xFe_{12-x}O_{19}$ with different Ce^{+3} concentration (x = 0.0, 0.25, 0.5, 0.75, and 1.0) is displayed.

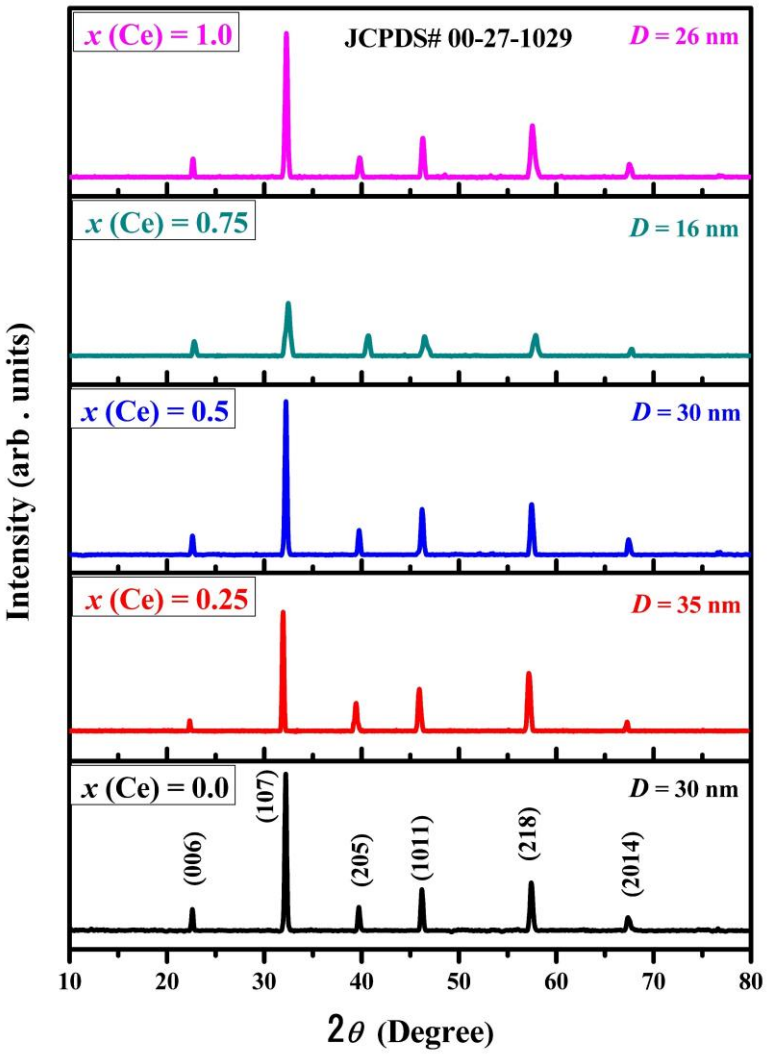

Figure 1: X-ray diffraction (XRD) analysis of cerium substituted barium hexaferrites $BaCe_xFe_{12-x}O_{19}$ (x = 0.0, 0.25, 0.5, 0.75, and 1.0) nanoparticles

Rietveld Refinement via Full Prof suit was also used to examine the X-Ray Diffraction pattern. The Rietveld refinement approach is a potential method for analyzing detailed crystal structure information from powder diffraction data. The Rietveld-refined diffraction XRD pattern of angle 10°–80°, annealed at 900 °C, is presented in (Figure 2).

All of the XRD patterns were studied using the Rietveld refinement approach in hexagonal symmetry with the P63/mmc space group. Different parameters were refined in sequence, such are background and scale factor, profile shape, width parameters, asymmetry atomic coordinate and site occupancies. The peak shape function is studied by using Pseudo-Voigt approximation which is the combination of Lorentzian and Gaussian component. The Rietveld refinement of XRD patterns of $BaCe_xFe_{12-x}O_{19}$ at (x = 0.0, 0.25, 0.5, 0.75, 1.0) is shown in (Figure 2). Where, the observed data is shown by a black solid circle, the calculated intensities by a red solid line, the Bragg's positions by vertical pink lines, and the bottom blue lines represents the difference between observed and calculated intensities. The successful Rietveld refinement is dependent on the peaks shape, the refinement results are not successful if peaks are not correctly described (Manglam, Kumari, Mallick, & Kar, 2021). However, the data we have well-resolved peaks in the diffraction pattern, where observed and calculated intensities are matching to each other, and also well matched with JCPDS card number 00-027-1029, which confirm the formation of BHF nanoparticles. The observed diffraction peaks corresponding to reflection planes (006), (107), (205), (1011), (218), and (2014) provide clear evidence for the formation of BHF nanoparticles.

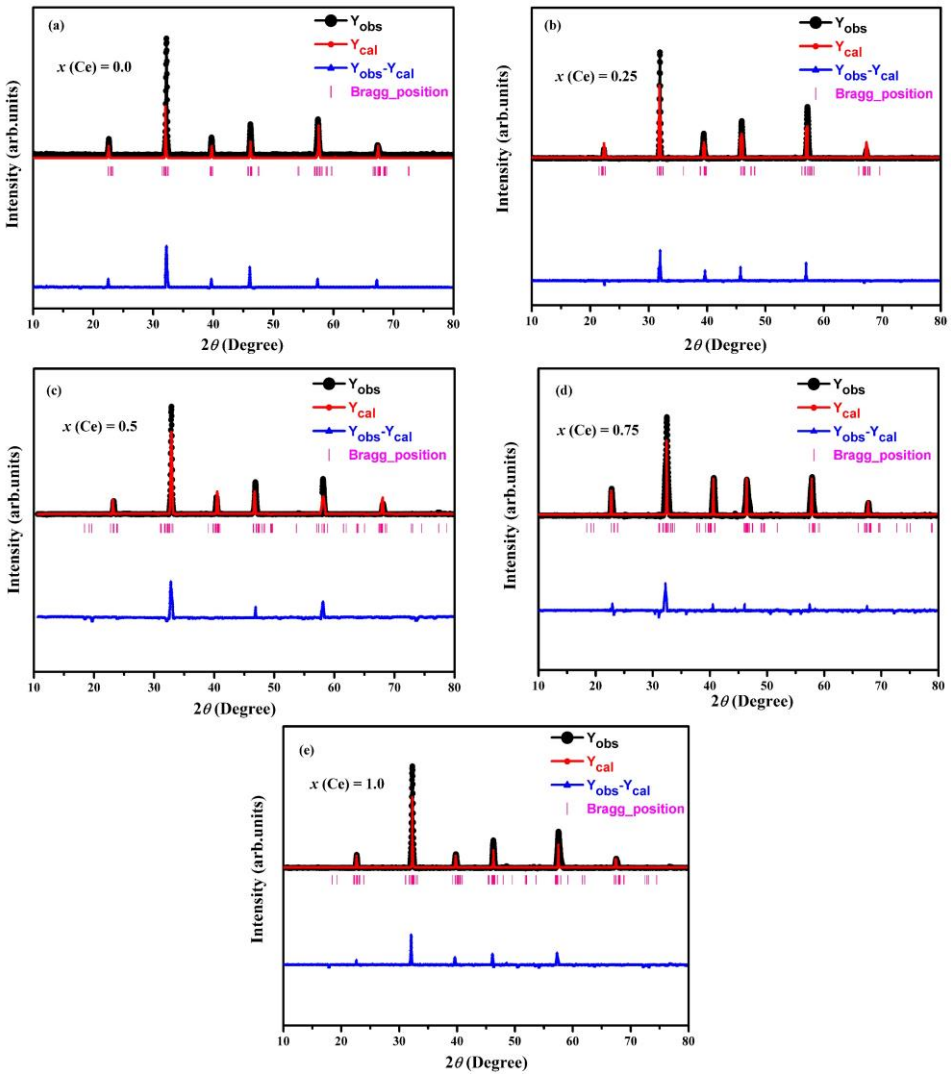

Figure 2: Rietveld refinement analysis of Ce^{+3} substituted barium hexaferrite $BaCe_xFe_{12-x}O_{19}$ (x = 0.0, 0.25, 0.5, 0.75, and 1.0) nanoparticles

The crystal structure obtained from Rietveld refined parameters by using Vesta software is shown in (Figure 3), where Ba atoms indicated as red, Fe atoms as light violet and oxygen as bark blue. The structure of BHF is covered with irons and oxygen layers, where iron atoms are arranged in tetrahedral and octahedral holes, excluding one set of Fe atoms which is linked with five O atoms. So, the BHF includes 18 octahedral, 4 tetrahedral, and 2 bipyramids Fe atoms in a single unit cell which is shown in (Figure 3), and the values of atomic parameter of Ce^{+3} substituted $BaFe_{12}O_{19}$ at (x = 0.0) is given in (Table 1).

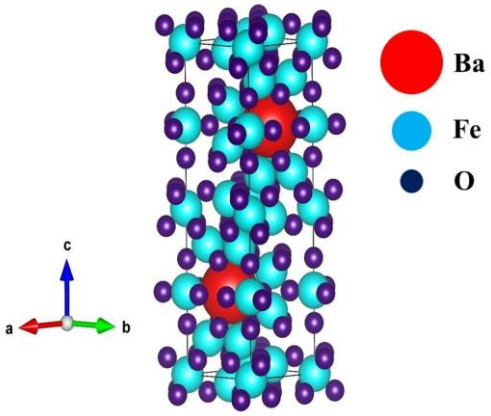

Figure 3: Schematic diagram of crystal structure of barium hexaferrite $BaFe_{12}O_{19}$ at (x = 0.0)

Table 1
Atomic parameter of the barium hexaferrite $BaFe_{12}O_{19}$ at (x = 0.0)

Atom	x	y	z	Occ	Site
Ba^{+2}	$^2/_3$	$^1/_3$	$^1/_4$	1	2d
$Fe^{+3}(1)$	0	0	0	1	2a
$Fe^{+3}(2)$	0	0	$^1/_4$	1	2b
$Fe^{+3}(3)$	$^1/_3$	$^2/_3$	0.028	1	4f
$Fe^{+3}(4)$	$^1/_3$	$^2/_3$	0.189	1	4f
$Fe^{+3}(5)$	0.166	$^1/_3$	0.108	1	12k
$O^{-2}(1)$	0	0	0.151	1	4e
$O^{-2}(2)$	$^1/_3$	$^2/_3$	0.055	1	4f
$O^{-2}(3)$	0.19	0.38	0.052	1	6h
$O^{-2}(4)$	0.16	0.32	$^1/_4$	1	12k
$O^{-2}(5)$	$^1/_2$	1	0.15	1	12k

The formula (1) is used to measure the lattice constants a and c of Ce^{+3} substituted $BaCe_xFe_{12-x}O_{19}$ nanoparticles:

$$\frac{1}{d_{hkl}^2} = \left[\frac{4}{3}\frac{h^2+hk+k^2}{a^2} + \frac{l^2}{c^2}\right] \quad (1)$$

Where a & c are lattice constants and d_{hkl} is the distance between planes (h k l). The average lattice constant a is estimated to be between 5.82 – 5.89 Å. The ionic radius of Ce^{3+} and Fe^{3+} is used to characterize variations in the 'a'. With the replacement of Ce^{3+} ion the lattice constant a is found to decrease, this is due to the octahedral site replacing a broad radius of Ce^{3+} ion (1.034 Å) with a smaller radius Fe^{3+} ion (0.64 Å). The lattice constant a reduces slightly with substitution and at that time increases, before gradually decreasing to the lowest value, which may be due to Ce^{3+} ion discrimination at grain boundaries (Chandrasekaran, Selvanandan, & Manivannane, 2004). While the lattice constant c found increase, as the concentration of Ce^{+3} increases. After (x = 0.5) it decreases till to (x = 0.75), than again rises to the highest value, which is due to Ce^{3+} ion resemblance at grain boundaries (Chandrasekaran et al., 2004). The lattice constant c is found to be between 23.13 – 23.42 Å. The variation in lattice constants a and c with respect to Ce^{+3} concentration is shown in (Figure 4).

The formula (2) is used to calculate the x-ray density ρ_x of the prepared nanoparticles:

$$\rho_x = 2M/N_A V \quad (2)$$

Where, M is the molecular weight (g/mol), N_A would be the Avogadro number (6.023×10^{23} mol^{-1}), and V seems to be the volume of an individual cells. The x-ray density is observed increasing from 5.29 – 5.76 g/cm^3 depending on the Ce^{+3} concentration. Which is attributed due to higher molar mass of Ce^{3+} (140.12 g/m) in a comparison with Fe^{3+} (55.845 g/m), so the x-ray density rises as the concentration of Ce^{3+} increases (Brightlin & Balamurugan, 2016).

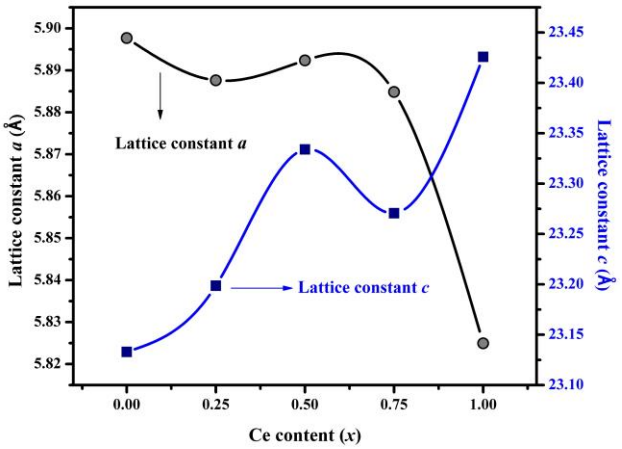

Figure 4: Variation in lattice constants *a* and *c* as a function of Ce^{+3} concentration (*x*) of $BaCe_xFe_{12-x}O_{19}$ (*x* = 0.0, 0.25, 0.5, 0.75, and 1.0) nanoparticles

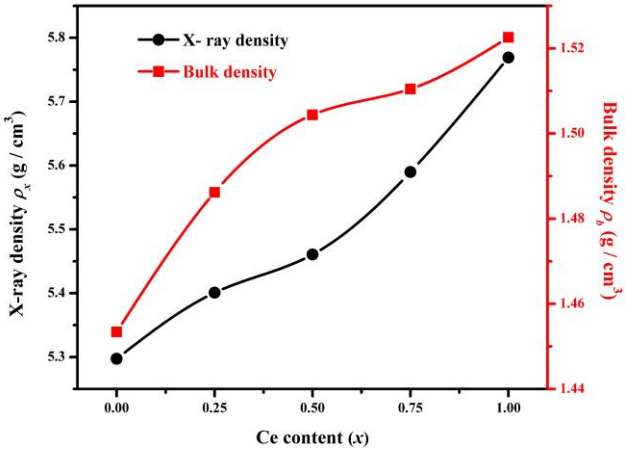

Figure 5: X-ray density ρ_x and bulk density ρ_b as a function of Ce^{+3} concentration (*x*) of $BaCe_xFe_{12-x}O_{19}$ (*x* = 0.0, 0.25, 0.5, 0.75, and 1.0) nanoparticles

The bulk density ρ_b of the organized pallets is measured by using the principle (3):

$$\rho_b = m_b/\pi r^2 h \quad (3)$$

Wherever, 'm_b' is the mass of the pellets, '*r*' is radius, and '*h*' is height. Bulk density is dependent on the molar mass of the doping element Ce^{+3} (140.12 g/m) and the increasing concentration (*x* = 0.0, 0.25, 0.5, 0.75, and 1.0). Bulk density is observed increases from 1.45 – 1.52 g/cm^3 as the concentration of Ce^{+3} increase. X-ray density is found to be higher than bulk density due to the creation of pores during sample preparation and annealing. X-ray density and bulk density with respect to Ce^{+3} concentration is shown in (Figure 5).

The volume of the unit cell *V* is calculated by using the formula (4):

$$V = \frac{\sqrt{3}}{2} a^2 c \quad (4)$$

Where *a* and *c* are the lattice constants. The cell volume values of cerium substituted barium hexaferrites $BaCe_xFe_{12-x}O_{19}$ nano particles at (*x* = 0.0, 0.25, 0.5, 0.75, and 1.0) is given in the (Table 2). The unit cell volume varies with different Ce^{+3} concentration, while at (*x* = 0.5) cell volume reaches to highest value. The cell volume is found to be in a range 688.35 – 701.61 Å^3.

The formula (5) is used to measure the stacking fault *SF* of the prepared nanoparticles:

$$\textbf{Stacking Fault (SF)} = 2\pi^2/45\sqrt{3}(\tan\theta) \quad (5)$$

Stacking fault is a planner defect and has a direct relation with 2θ and has inverse relation with β. of stacking fault with respect to Ce^{+3} concentration shows inhomogeneous behavior, where stacking fault first rises then decreases to lowest value and then again increases at (x = 1.0), This inhomogeneous behavior can be due to annealing temperature (Brightlin & Balamurugan, 2016). Stacking fault is found to be between 0.469 – 0.473. Variation in cell volume $Å^3$ and stacking fault with respect to Ce^{+3} concentration is shown in (Figure 6). Values of XRD parameters (lattice constants a and c, x-ray density ρ_x, bulk density ρ_b, cell volume ($Å^3$) and stacking fault) with respect to Ce^{+3} concentration (x = 0.0, 0.25, 0.5, 0.75, and 1.0) are given in the (Table 2).

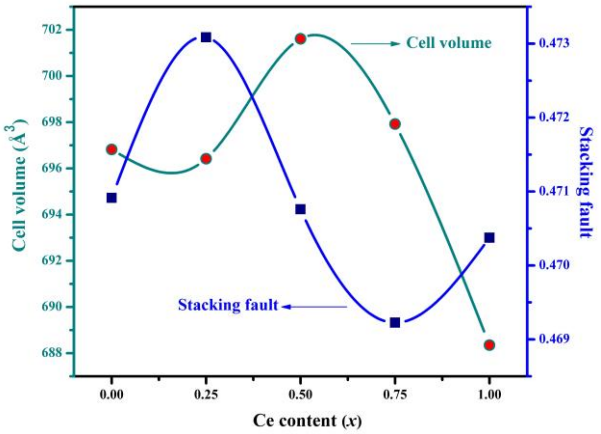

Figure 6: Variation in cell volume $Å^3$ and stacking fault as a function of Ce^{+3} concentration (x) of $BaCe_xFe_{12-x}O_{19}$ (x = 0.0, 0.25, 0.5, 0.75, and 1.0) nanoparticles

Table 2
Structural parameters: lattice constants a and c, x-ray density ρ_x, bulk density ρ_b, cell volume ($Å^3$), stacking fault of cerium substituted barium hexaferrites $BaCe_xFe_{12-x}O_{19}$ nanoparticles at (x = 0.0, 0.25. 0.5, 0.75, and 1.0)

Parameters	x = 0.0	x = 0.25	x = 0.5	x = 0.75	x = 1.0
Lattice constant a (Å)	5.89	5.88	5.89	5.88	5.82
Lattice constant c (Å)	23.13	23.19	23.33	23.27	23.42
X-ray density ρ_x (g / cm^3)	5.29	5.40	5.46	5.58	5.76
Bulk density ρ_b (g / cm^3)	1.45	1.48	1.50	1.51	1.52
Cell volume ($Å^3$)	696	696	701	697	688
Stacking fault	0.471	0.473	0.471	0.469	0.470

3.2. Crystalline Size and Strain

The crystalline size of $BaCe_xFe_{12-x}O_{19}$ nanoparticle have been calculated using the Debye Scherer method, Williamson-Hall (W-H) method and size-strain plot (SSP) method, which provides better understanding about crystallite size and lattice strain contributions (Tetiana Tatarchuk et al., 2020).

Using Debye Scherrer equation (6), the crystallite size D of Ce^{+3} doped $BaCe_xFe_{12-x}O_{19}$ particles was calculated from the sharpest and strongest peak at (107) *hkl* of x-ray diffraction patterns (Mozaffari, Amighian, & Darsheshdar, 2014). Debye Scherrer:

$$\boldsymbol{D = k\lambda/(\beta\, cos\theta)} \quad (6)$$

The constant is denoted by K with a value of 0.89, and the wavelength of the x-ray beam is denoted by λ with a value of 1.54 Å. β is the full width at half maximum (FWHM) at *hkl* (107) and the angle of diffraction is denoted by θ. The crystalline size was found to be in a range between 16 – 35 nm is shown in (Figure 7). This crystallite size is observed smaller as compared to the other reported rare earth doped barium ferrites. As per Bragg's

law the crystalline size has direct relation with 2θ and inverse relation with β. The crystalline size varies in a similar way with the substitution of Ce^{3+} contents. This inhomogeneous behavior may be larger ionic radius of Ce^{+3} ion (1.034 Å) which was replaced by small ionic radius of Fe^{3+} ions (0.64 Å) on the octahedral sites (Gilani, Warsi, Anjum, et al., 2015). The smallest crystalline size is observed 16 nm at (x = 0.75) due to β of the intense peak.

The Stokes-Wilson equation (Reddy, Babu, Reddy, & Shim, 2018) is used to calculate the lattice strain ε_L of the prepared nanoparticles:

$$\boldsymbol{\varepsilon_L = \beta_{hkl}/4\,tan\,\theta\,(10)^{-3}} \quad (7)$$

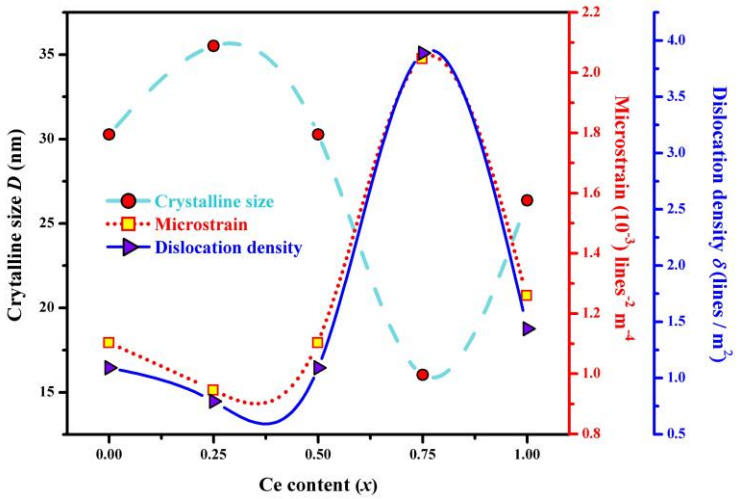

Figure 7: Variation in crystalline size *D* by Debye Scherrer (SM) method, microstrain ε and dislocation density δ as a function of Ce^{+3} concentration (*x*) of $BaCe_xFe_{12-x}O_{19}$ (*x* = 0.0, 0.25, 0.5, 0.75, and 1.0) nanoparticles

Where, β is the full width half maximum (FWHM) of the intense peaks. The microstrain ε_M of prepared nanoparticles is calculated from the equation (8):

$$\boldsymbol{\varepsilon_M = (\beta^{*}\,cos\,\theta)/4(10)^{-3}} \quad (8)$$

Lattice strain is the disturbance of lattice constants, such as lattice dislocations, which arise from crystal imperfection, while microstrain is the root mean square of variations in the lattice parameters across samples. Lattice strain and microstrain has direct relation with β (crystalline size) and inverse relation with 2θ. The lattice strain is observed between 3.50 – 7.65 x 10^{-3}, while microstrain is found between 0.96–2.13 x 10^{-3} ($lines^{-2}/m^{-4}$). In (Figure 7) It is estimated that the microstrain is slightly declining at first, then gradually increasing at the peak stage and then decreasing again. The maximum value of microstrain is observed at (x = 0.75), which indicates that the crystalline size is minimum and 2θ is maximum at that point.

Dislocation density of the prepared nanoparticles is calculated by using the formula:

$$\boldsymbol{\delta = 1\,/D^2} \quad (9)$$

The crystalline scale is denoted by *D*. Dislocation density also has inverse relation with crystalline size. The density of dislocations is found to be between 0.79 – 3.88 x 10^{15} (lines / m^2). It is discovered that first it decreases to lowest value than rises in proportion to the substituent concentration. At (x = 0.75), the maximal value of dislocation density is found, which shows the crystalline size *D* is minimum at that point. The variation in crystalline size *D* by Debye Scherrer (SM), microstrain ε and dislocation density δ as a function of Ce^{+3} concentration is shown in (Figure 7).

The crystalline size is also estimated by using Williamson–Hall method (Kumar & Kar, 2016). In the W–H technique, the line broadening attributable to the finite size of the coherent scattering region and the internal stress in the prepared film are also taken into account. The diffraction line widening, according to Williamson and Hall, is caused by crystallite size and strain contribution. The W–H approach is a basic method that uses the peak width as a function of 2θ to distinguish between size-induced and strain-induced peak broadening (Bindu & Thomas, 2014). According to Williamson–Hall (W–H) method, the sum of the contributions of crystallite size and strain present in the material is the overall peak broadening, which can be stated as (10): (Biju, Sugathan, Vrinda, & Salini, 2008).

$$\boldsymbol{\beta_{hkl} = \beta_D + \beta_\varepsilon} \quad (10)$$

Where, β_D is the contribution of crystalline size using equation (6), while β_ε is the strain induced, due to crystal imperfection and distortion using equation (Bindu & Thomas, 2014). The sum of equations (6) and (Bindu & Thomas, 2014) is given as (11):

$$\boldsymbol{\beta_{hkl} = \frac{k\lambda}{\beta cos\theta} + 4\,\varepsilon\, tan\theta} \quad (11)$$

Rearranging the equation (11) we get equation (12):

$$\boldsymbol{\beta_{hkl} cos\theta_{hkl} = \frac{k\lambda}{D_{WH}} + 4\,\varepsilon\, sin\theta_{hkl}} \quad (12)$$

Where, ε is microstrain, which was estimated from slope of the linear fit, while D_{WH} is the crystalline size estimated from the y-intercept ($k\lambda/D_{WH}$). The liner graph is plotted between $\beta_{hkl}\cos\theta$ vs $4\sin\theta_{jkl}$. Using Williamson–Hall method the crystalline size is found to be between 19–68 nm and the correlation coefficient is (R^2 = 1.00) for all the samples. The plot of Williamson-Hall (W-H) method of Ce^{+3} substituted $BaCe_xFe_{12-x}O_{19}$ at (x = 0.0, 0.25, 0.5, 0.75, 1.0) is shown in (Figure 8), and the values of crystalline size $D_{W\text{-}H}$ and microstrain ε_M is given in (Table 3).

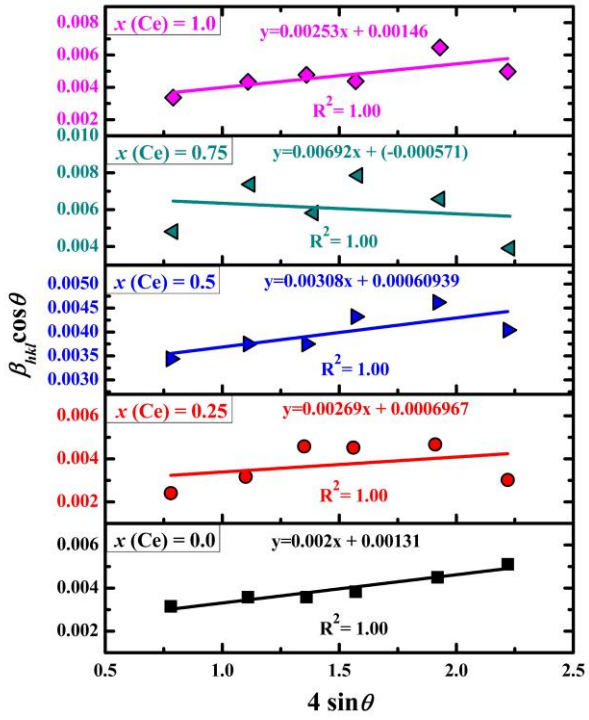

Figure 8: Plot of $\beta_{hkl}\cos\theta$ versus $4\sin\theta_{hkl}$ of Ce^{+3} substituted $BaCe_xFe_{12-x}O_{19}$ (x = 0.0, 0.25, 0.5, 0.75, and 1.0) nanoparticles by Williamson–Hall (W–H) method

As per W–H plots, the line broadening was almost isotropic, this emphasizes that the diffracting domains were isotropic, which is attributed due to the contribution of microstrain. In the case of isotropic line broadening, an average size–strain plot (SSP) can be used to provide a better estimate of the size–strain parameters.(Bindu & Thomas, 2014)

This approach has the advantage of giving less importance to data from high-angle reflections, where accuracy is often less. In this method, profile corresponding to crystallite size is explained by a Lorentz function and the profile corresponding to strain is explained by a Gaussian function (Tetiana Tatarchuk et al., 2017; Zak, Majid, Abrishami, & Yousefi, 2011) and is given by (13):

$$(\boldsymbol{d_{hkl}} \times \boldsymbol{\beta_{hkl}} \times \boldsymbol{\cos\theta})^2 = \frac{k\lambda}{D_{SSP}} \times (\boldsymbol{d_{hkl}^2} \times \boldsymbol{\beta_{hkl}} \times \boldsymbol{\cos\theta}) + \frac{\varepsilon^2}{4} \quad (13)$$

where d_{hkl} is the interplanar spacing, the distance between (hkl) planes, k is constant having a value of 0.89 and λ is 0.15406 (nm). D_{SSP} is the apparent volume weighted average crystalline size and ε is the apparent strain. The liner graph is plotted between $(d_{hkl}\ \beta_{hkl}\ \cos\theta_{hkl})^2$ on y-axis and $(d_{hkl}^2\ \beta_{hkl}\ \cos\theta_{hkl})$ on x-axis.

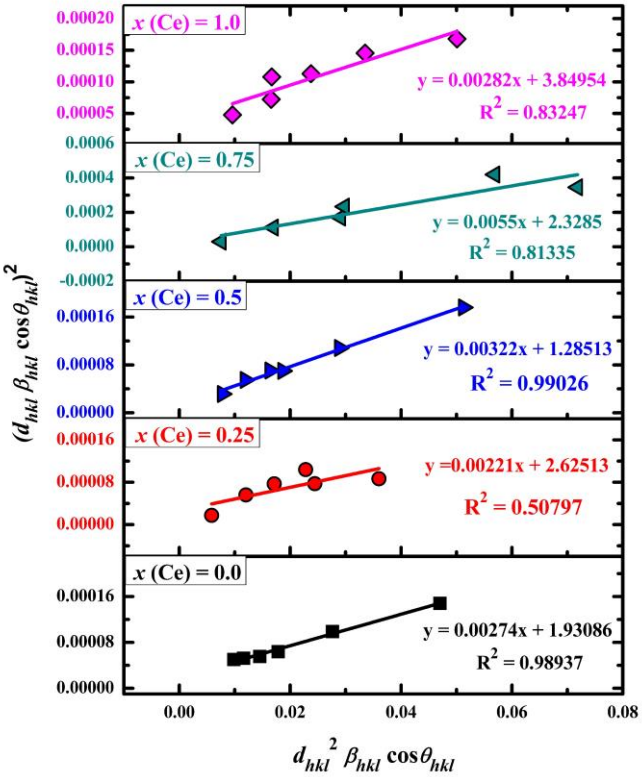

Figure 9: Plot of $(d_{hkl}\beta_{hkl}\cos\theta_{hkl})^2$ versus $d_{hkl}^2\beta_{hkl}\cos\theta_{hkl}$ of Ce^{+3} substituted $BaCe_xFe_{12-x}O_{19}$ (x = 0.0, 0.25, 0.5, 0.75, and 1.0) nanoparticles by Size–Strain Plot (SSP) method

All the peaks of $BaCe_xFe_{12-x}O_{19}$ hexagonal ferrites are under 2θ = 20° – 80°. The average crystalline size was estimated from the slop of the liner fit and the strain ε is estimated from the intercept respectively. It is observed that crystalline size is decreasing with increasing Ce^{+3} concentration. The value of crystalline size varying in the range 24– 62 nm and the correlation coefficient varies in the range of (R^2 = 0.50797–0.99026). The size-strain plot (SSP) method of Ce^{+3} substituted $BaCe_xFe_{12-x}O_{19}$ is shown in (Figure 9). The crystalline size obtained from Scherrer method is smaller than compare to W–H method and SSP method. The smallest crystalline size obtained from Scherrer method is 16 nm, while in W–H method the smallest crystalline size is 19 nm, and 24 in SSP method. However, the average crystalline sizes in SSP method are the most suitable one compared to W–H method. The reason behind large crystalline size in W-H and SSP method is due to strain contribution (Şelte & Özkal, 2019). In Debye Scherrer method we consider only FWHM of the most intense peak, while in W-H and SSP method we take average crystalline size from all the peaks, which also includes strain contribution. The magnitude of crystallite size in these 3 models is in agreement with the peak intensities obtained from XRD analysis (Figure 1). The values of crystalline size $D_{W\text{-}H,}$ lattice strain ε_L, microstrain ε_M and dislocation density δ of barium hexaferrite $BaCe_xFe_{12-x}O_{19}$ nanoparticles, calculated via Debye Scherrer

(SM) method, Williamson-Hall (W-H) method and size-strain plot (SSP) method is given in (Table 3).

Table 3
Crystalline size D_{W-H}, lattice strain ε_L, microstrain ε_M and dislocation density δ of barium hexaferrite $BaCe_xFe_{12-x}O_{19}$ nanoparticles, calculated by Debye Scherrer (SM) method, Williamson-Hall (W-H) method and size-strain plot (SSP) method

Composition	SM method				W–H method			SSP method		
x (Ce^{+3})	D_{SM},nm	$\varepsilon_L\times10^{-3}$	$\varepsilon_M\times10^{-3}$	$\delta\times10^{15}$	D_{W-H}, nm	$\varepsilon_M\times10^{-3}$	δ	D_{W-H}, nm	$\varepsilon_M\times10^{-3}$	δ
x (Ce) = 0.0	30	4.08	1.13	1.09	68	6.1	0.0002	50	1.9	0.0004
x (Ce) = 0.25	35	3.50	0.96	0.79	50	6.9	0.0004	62	3.2	0.0002
x (Ce) = 0.5	30	4.07	1.13	1.09	44	6.1	0.0005	42	2.3	0.0006
x (Ce) = 0.75	16	7.65	2.13	3.88	19	-5.7	0.003	24	3.1	0.002
x (Ce) = 1.0	26	4.67	1.29	1.43	54	4.6	0.0003	48	3.9	0.0004

3.3. FTIR Analysis

The Fourier transform infrared spectrum (FTIR) is performed on the IS50 FT-IR. FTIR is an important instrument used to determine the internal structure of the prepared samples. The prepared ferrites having compositional formula $BaCe_xFe_{12-x}O_{19}$ (x = 0.0, 0.25, 0.5, 0.75, and 1.0) are investigated. FTIR spectra of Ce^{+3} substituted $BaCe_xFe_{12-x}O_{19}$ is seen in the (Figure 10), and were recorded in the range of 390 –1000 cm^{-1}. The two absorption bands below 700 cm^{-1} have been observed in FTIR analysis and are assigned as ν_1 and ν_2. The high frequency band ν_1 observed in a span of 500 – 620 cm^{-1}, representing tetrahedral A-site stretching bands and the low frequency band ν_2 observed in a span of 400– 500 cm^{-1}, representing octahedral B-site stretching bands. These frequency bands represent the characteristic feature of hexagonal structure. The changes in both ν_1 and ν_2 is observed. The octahedral and tetrahedral stretching bands are responsible for two absorption bands of hexagonal ferrites (Raju & Murthy, 2013). Intrinsic vibrations at tetrahedral A-sites are responsible for the first absorption band ν_1, while the intrinsic vibrations at octahedral B-sites are responsible for the second absorption band ν_2 (Wang & Hu, 2005). The high frequency bands (533.7 cm^{-1}, 534 cm^{-1}, 538 cm^{-1}, 535 cm^{-1}, 534 cm^{-1}) and low frequency bands (411 cm^{-1}, 412.4 cm^{-1}, 410.1 cm^{-1}, 411 cm^{-1}, 412.9 cm^{-1}) are formed because of the Fe^{3+}–O^{2-} stretching vibrations at tetrahedral and octahedral site.

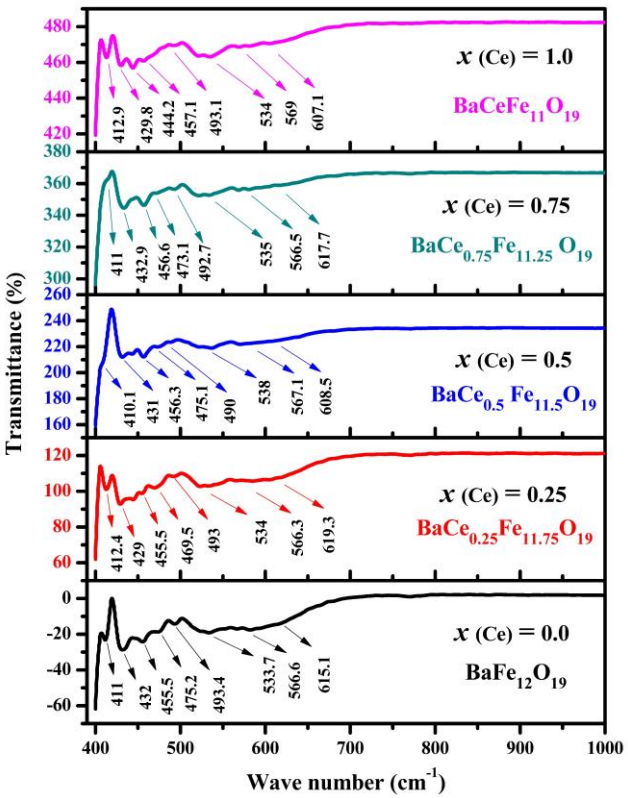

Figure 10: The IR-spectra of Ce^{+3} substituted $BaCe_xFe_{12-x}O_{19}$ (x = 0.0, 0.25, 0.5, 0.75, and 1.0) nanoparticles annealed at 900°C

The values of ν_1 is greater than those of ν_2, suggesting that the tetrahedral vibration site is greater than that of the corresponding octahedral sites. This might be because of tetrahedral A-site has a shorter bond length than the octahedral B-site. The variation in tetrahedral ν_1 and octahedral ν_2 absorption peaks is due to the variation generated in the grain size and lattice parameters by increasing Ce^{+3} Contents, and these changes affect the stretching vibrations of Fe^{3+}–O^{2-} due to which the band position may be changed (Gilani, Warsi, Khan, et al., 2015; Junaid et al., 2016). The peaks beyond 1000 cm^{-1} were due to H–O–H stretching vibrations of absorbed water molecules (Karimi et al., 2014).

The force constant is an important characteristic of chemical bonds in hexagonal structure. According to researcher, (Lakhani, Pathak, Vasoya, & Modi, 2011) the force constants octahedral site K_O and tetrahedral site K_T of the samples are calculated from the ν_1 and ν_2 values by using the formulas (14) and (15):

$$\boldsymbol{K_O = 0.942128M\,(\nu_2)^2/\,(M+32)} \quad (14)$$

$$\boldsymbol{K_T = \sqrt{2K_o\nu_1/\nu_2}} \quad (15)$$

Where M is the molecular weight, ν_1 and ν_2 is frequency bands. The force constants are examined in order to increase the doping concentration, which in-dictates that interionic bonding may be strengthened. It is observed that the force constant K_O varies at different concentrations, while the force constant K_T is increases up to (x = 0.75) and after that decreases with increasing Ce^{+3} concentration. The bond length is known to be inversely proportional to the force constant. (TR Tatarchuk, Bououdina, Paliychuk, Yaremiy, & Moklyak, 2017) The relationship between bond lengths and force constants as a function of Ce^{+3} concentration is shown in Figure 11(a) and Figure 11(b), where bond lengths are taken in nanometers. The bond lengths octahedral B-site (M_B-O) and tetrahedral A-site (M_A-O) of the prepared particles is determined using the equation (16) (Muneer, Farrukh, & Raza, 2020):

$$\boldsymbol{r = \sqrt[3]{17}/K} \quad (16)$$

Where K is the force constants K_O and K_T, which are calculated from the equations (14) and (15). The inverse relationship between force constants K_O and K_T with octahedral (M_B-O) and tetrahedral (M_A-O) bond lengths are confirmed. Therefore, the chemical bond strengths rise as the distance between the atoms is decreases, resulting in an increase in the force constants values. In (Table 4) the computed values of force constants K_O and K_T, bond lengths (M_B-O) and (M_A-O) are mentioned.

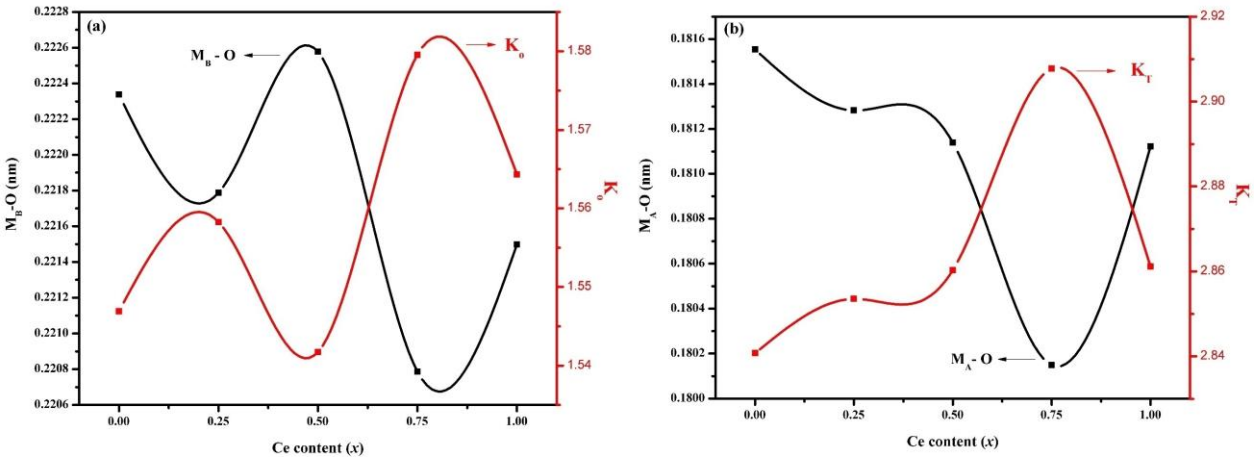

Figure 11: (a) Correlation between octahedral B-site (M_B-O) bond length and force constant (K_O) as a function of Ce^{+3} concentration (b) Correlation between tetrahedral A-site (M_A-O) bond length and force constant (K_T) as a function of Ce^{+3} concentration

Table 4
Molecular weights, IR bands, force constants (K_o and K_t), bond lengths (M_B-O and M_A-O) of cerium substituted barium hexaferrites $BaCe_xFe_{12-x}O_{19}$ nanoparticles at (x = 0.0, 0.25. 0.5, 0.75, and 1.0)

Parameters	x = 0.0	x = 0.25	x = 0.5	x = 0.75	x = 1.0
Molecular weight (gm/mol)	1111.47	1132.54	1153.61	1174.68	1195.75
ν_1 (cm^{-1})	533.7	534	538	535	534
ν_2 (cm^{-2})	411	412.4	410.1	411	412.9
$K_O \times 10^5$ (dyne/cm^2)	1.54691	1.55828	1.54172	1.57955	1.56433
$K_T \times 10^5$ (dyne/cm^2)	2.84076	2.85353	2.8603	2.90777	2.86114
M_B-O (Å)	2.22339	2.21787	2.22578	2.20787	2.21499
M_A-O (Å)	1.81554	1.81283	1.81139	1.80149	1.81122

3.4. Dielectric Analysis

The dielectric properties are one of the important features, especially for ferrites in order to unfold their suitability for high frequency devices applications. These properties depend upon materials composition, method of preparation and cation positions in the unit cell (Gilani, Warsi, Anjum, et al., 2015). The dielectric properties of prepared ferrite samples with the general formula $BaCe_xFe_{12-x}O_{19}$ at (x = 0.0, 0.25, 0.5, 0.75, and 1.0) are performed at room temperature using an impedance analyzer over a frequency range of 1 MHz – 3 GHz. The dielectric constant, dielectric loss, tangent loss, AC conductivity, the real-imaginary impedance, and the real-imaginary modulus of $BaCe_xFe_{12-x}O_{19}$ (x = 0.0, 0.25, 0.5, 0.75, and 1.0) ferrites were investigated.

3.4.1. Dielectric Constant and Dielectric Loss

The dielectric constant (ε') and dielectric loss (ε'') of prepared cerium substituted barium hexaferrites $BaCe_xFe_{12-x}O_{19}$ nanoparticles are calculated with respect to the frequency of applied field by using the formulas (17) and (18):

$$\varepsilon' = \frac{t}{\omega A \varepsilon_o} \frac{z''}{z^2+z'^2} \quad (17)$$

$$\varepsilon'' = \frac{t}{\omega A \varepsilon_o} \frac{z'}{z^2+z'^2} \quad (18)$$

Where t represents pallet thickness, ω is the angular frequency of the applied AC signal, A represents pallet surface area, and ε_o signifies the permittivity of free space (8.85×10^{-12}).

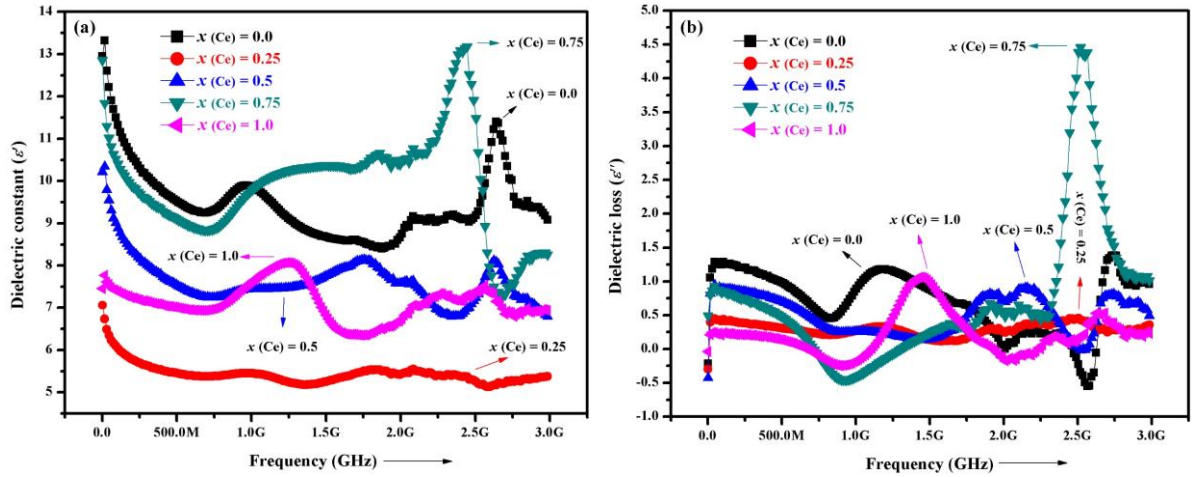

Figure 12: (a) Variations in real component of dielectric constant of $BaCe_xFe_{12-x}O_{19}$ (x = 0.0, 0.25, 0.5, 0.75, and 1.0) nanoparticles as a function of frequency (b) Variations in imaginary component of dielectric loss of $BaCe_xFe_{12-x}O_{19}$ (x = 0.0, 0.25, 0.5, 0.75, and 1.0) nanoparticles as a function of frequency

The dielectric constant as a function of frequency is shown in Figure 12(a). The observations revealed that the dielectric constant is decreasing by increasing frequency up to 1 GHz. After 1 GHz, most of compositions increases by increasing frequency. The decrease in dielectric constant is attributed due to dispersion phenomenon. Which occurs due to changes in polarization as a function of applied field at low frequency. However, such behavior is not observed at high frequency. These ferrites exhibit such behavior due to Maxwell Wagner interfacial polarization and Koop's phenomenological theory (Redinz, 2011). These phenomenon's states that grains are more effective by high frequencies and grain boundaries have a significant impact on short frequencies, which is due to the space charge effect. At low frequency the electrons are gathered at grain boundaries, so the dielectric constant reaches to highest value. As frequency increases, the dielectric constant decreases, where hopping frequency does not match the functional frequency, so the ferric ions occupy the octahedral site resulting in a ferric ion deficiency, and the dielectric constant is reduced due to the electron exchange between Fe^{3+} and Fe^{2+} (Tetiana Tatarchuk et al., 2020). Ferromagnetic resonance is another name for this phenomenon. After at 2.5 GHz the dielectric constant again increases, since hopping frequency follows the applied field frequency. The highest value of dielectric constant among all the compositions is observed at (x = 0.75) on frequency range of 2.5 GHz. The dielectric loss as a function of frequency is shown in Figure 12(b). Variations in dielectric loss is observed same like in dielectric constant. Almost two relaxation peaks are found in all compositions, lower relaxation peak is found around at 1 GHz, which is due to interfacial or space charge distribution, and the higher relaxation peak is found around 2.5 GHz, which is due to ionic relaxation of ions with multiple valences. Some of other variations is also seen with different doping concentrations following hopping phenomenon (M. A. Khan et al., 2014). The highest value of dielectric loss is found on (x = 0.75) composition at frequency of 2.5 GHz. The values of dielectric constant (ε') and dielectric loss (ε'') from 1 MHz – 3GHz are given in (Table 5).

3.4.2.Tangent Loss and AC Conductivity

The Tangent loss (Tan δ) is the rate of energy loss in the dielectric materials. It is related to dielectric constant (ε') and dielectric loss (ε'') as per following formula (19):

$$(\boldsymbol{tan\,\delta = \varepsilon''/\varepsilon'}) \tag{19}$$

In case of tangent loss, increasing and decreasing at various frequencies are seen. We observed that tangent loss comparatively high at low frequency, which shows electron hopping frequency follows the applied field frequency. But soon at 1 GHz, the tangent loss apparently decreases due to electron hopping between Fe^{2+}– Fe^{3+} doesn't follow the applied field frequency (Sheikh et al., 2019). At 1.5 GHz the fifth sample (x = 1.0) in tangent loss reaches to maximum value, and at 2.5 GHz the fourth sample (x = 0.75) reaches to maximum value, where electron hopping frequency following the applied field frequency. These variation in value of tangent loss is explained grain boundaries, impurities and density of samples. According to Maxwell–Wagner theory tangent loss is inversely proportional with the frequency. From Figure 13(a) it is clear that when the frequency increases so the tangent loss decreases and somehow it shows variations (up-down) peaks. The values of tangent loss (Tanδ) from 1 MHz – 3GHz are given in (Table 5).

One of the most important properties of a dielectric analysis is its alternating current (AC) conductivity, taken in a frequency range of 1 MHz – 3 GHz. The AC conductivity of the prepared cerium doped barium hexaferrites $BaCe_xFe_{12-x}O_{19}$ nanoparticles at (x = 0.0, 0.25, 0.5, 0.75, and 1.0) is determined. Formula (20) is used to calculate the AC conductivity:

$$\boldsymbol{\sigma_{ac} = (t/A).z'/(z'^2 + z''^2)} \tag{20}$$

Where t denotes the width of the pallet, A its area, z' real impedance, and z'' imaginary impedance, respectively. The graph of variances in AC conductivity as a function of frequency for each of prepared samples is shown in Figure 13(b). The AC conductivity of the majority of samples has a growing pattern in the low frequency range. Soon at high frequency range of 1.5 GHz, it exhibits dispersive behavior, especially at the doping

element (x = 1.0) which shows high dispersion at 1.5 GHz. Both the Maxwell Wagner model and Koop's phenomenological theory clarifies that the ferrites materials consist of conducting grains which are separated by resistive layer of grain boundaries (Sheikh et al., 2019).

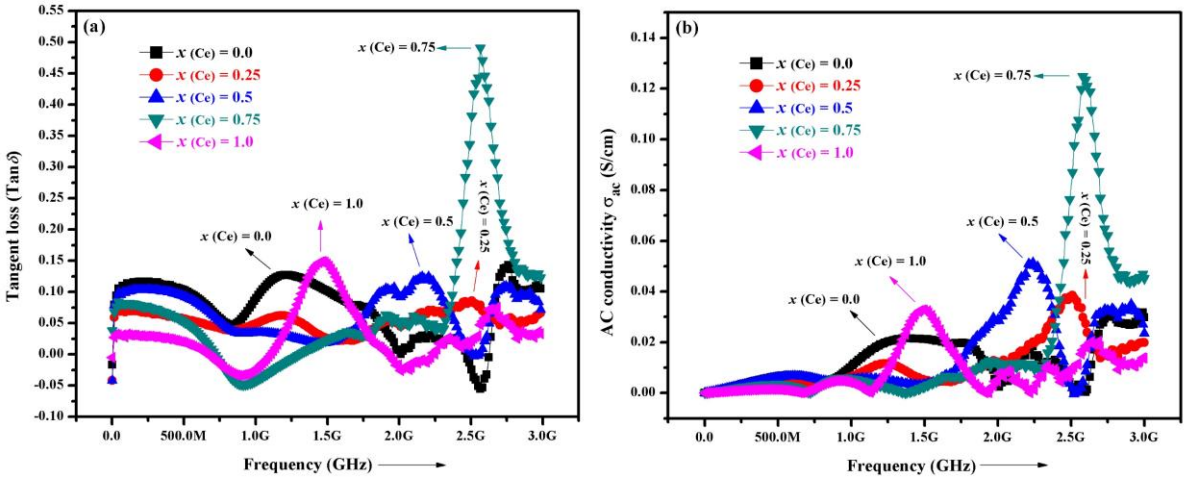

Figure 13: (a) Variations in tangent loss of $BaCe_xFe_{12-x}O_{19}$ (x = 0.0, 0.25, 0.5, 0.75, and 1.0) nanoparticles as a function of frequency (b) Variations in alternating current (AC) conductivity of $BaCe_xFe_{12-x}O_{19}$ (x = 0.0, 0.25, 0.5, 0.75, and 1.0) nanoparticles as a function of frequency

The conduction and dielectric polarization process are related to each other, so the actions of all samples tend to be planar and constant at low frequencies. The conductivity of Fe^{2+} and Fe^{3+} at octahedral sites is increased at high frequencies due to the properties of grains and hopping phenomena. The loss in porosity may also be behind the increase in conductivity. At low frequencies it is seen that the conductivity has a grain boundary effect whereas in the high frequency range the conducting effects of grains are observed, resulting in a dispersion pattern (Farid, Ahmad, Murtaza, Ali, & Ahmad, 2016; Gilani, Warsi, Anjum, et al., 2015; Junaid et al., 2016). The values of AC conductivity (σ_{ac}) from 1 MHz –3 GHz are given in the (Table 5).

Table 5

Measured values of dielectric constant (ε'), dielectric loss (ε'') tangent loss (Tan δ) and AC conductivity (σ_{ac}) of cerium substituted barium hexaferrites $BaCe_xFe_{12-x}O_{19}$ nanoparticles at (x = 0.0, 0.25, 0.5, 0.75, and 1.0) in the frequency range from 1 MHz – 3 GHz

Parameters	Frequency	x = 0.0	x = 0.25	x = 0.5	x = 0.75	x = 1.0
	1 MHz	12.95	7.06	10.21	12.85	7.46
	1 GHz	9.87	5.45	7.45	9.79	7.63
(ε')	2.5 GHz	9.19	5.25	7.24	11.48	7.4
	3 GHz	9.1	5.38	6.83	8.33	6.97
	1 MHz	0.29	0.21	0.08	0.99	0.47
	1 GHZ	1.4	0.78	0.77	0.1	0.34
(ε'')	2.5 GHz	0.28	0.96	0.53	4.89	0.67
	3 GHz	0.88	0.56	0.43	0.96	0.21
	1 MHz	0.03	0.01	0.01	0.09	0.04
	1 GHz	0.14	0.09	0.08	0.01	0.03
(Tan δ)	2.5 GHz	0.03	0.14	0.05	0.43	0.07
	3 GHz	0.09	0.06	0.06	0.11	0.02
	1 MHz	8.2E-07	8.9E-06	6.4E-06	3.8E-06	4.6E-06
	1 GHz	0.011	0.0065	0.0054	0.0055	0.0039
σ_{ac} (S/cm)	2.5 GHz	0.0023	0.0386	0.0019	0.0868	0.0092
	3 GHz	0.029	0.019	0.023	0.045	0.014

3.4.3.The Real and Imaginary Impedance

Impedance analysis is a valuable method for measuring the interaction between dielectric properties and microstructural structure of synthesized materials. For each of the ferrite $BaCe_xFe_{12-x}O_{19}$ at (x = 0.0, 0.25, 0.5, 0.75, and 1.0), the real and imaginary

impedance are measured in a range of 1 MHz – 3 GHz. Real and imaginary parts of impedance are calculated by the formulas (21) and (22):

$$Z' = R = |Z| \cos \theta_z \quad (21)$$
$$Z'' = X = |Z| \sin \theta_z \quad (22)$$

Where Z' is real impedance, while Z'' is imaginary impedance. Impedance spectrum shows that the increase of applied frequency reduces the real and imaginary impedance parts as seen in Figure 14(a) and Figure 14(b). These impedance parts are highly depending on the applied field frequency. The impedance curves of all samples (Real and Imaginary) converged as the frequency increases. At high frequencies, impedance curves of real impedance Z' and imaginary impedance Z'' merge with each other and shows constant behavior, which is attributed to the release of space charges (Joshi, Kanchan, Joshi, Jethva, & Parikh, 2017). These space charges are formed as a result of the concentration difference as well as the inhomogeneity of the applied field, which causes these charges to accrue on grain boundaries. With the increase of field frequency, the real and imaginary impedance decreases, indicating that conductivity improves (Joshi et al., 2017). The values of real and imaginary impedance from 1 MHz – 3GHz are given in (Table 6).

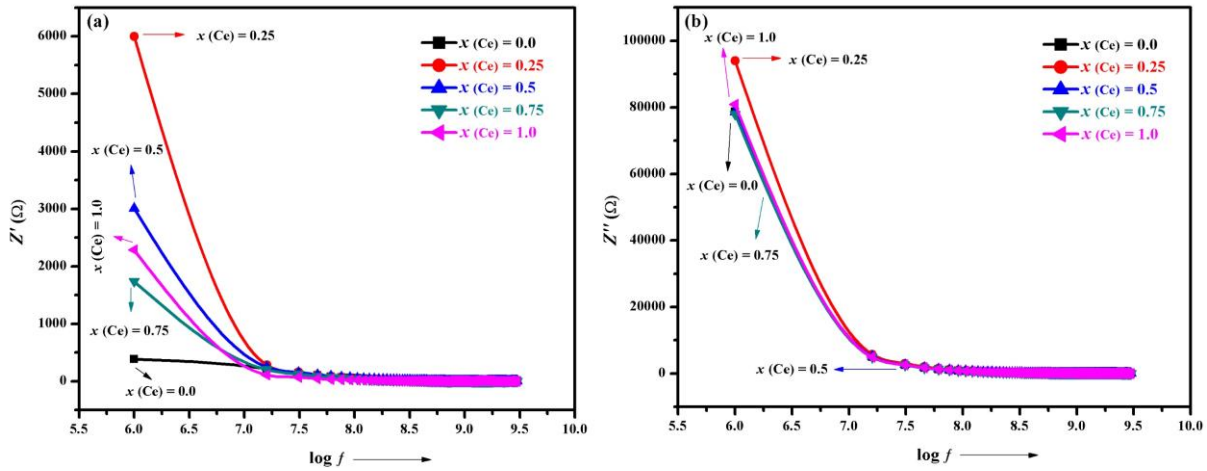

Figure 14: (a) Real part of Impedance of $BaCe_xFe_{12-x}O_{19}$ (x = 0.0, 0.25, 0.5, 0.75, and 1.0) nanoparticles as a function of log of frequency (b) Imaginary part of Impedance of $BaCe_xFe_{12-x}O_{19}$ (x = 0.0, 0.25, 0.5, 0.75, and 1.0) nanoparticles as a function of log of frequency

3.4.4.The Real and Imaginary Modulus

The function of grains and grain boundaries by a specified frequency range is investigated using modulus properties. The real and imaginary modulus of the prepared hexagonal ferrite with the composition formula as per a function of functional frequency $BaCe_xFe_{12-x}O_{19}$ (x = 0.0, 0.25, 0.5, 0.75, and 1.0) was determined. This property can be used to study the frequency dependent interfacial polarization effects, conduction, and relaxation behavior of hexagonal ferrites. The real and imaginary electric modulus are calculated using the following relationships (23) and (24):

$$M' = \varepsilon' / (\varepsilon'^2 + \varepsilon''^2) \quad (23)$$
$$M'' = \varepsilon'' / (\varepsilon'^2 + \varepsilon''^2) \quad (24)$$

Where M' is real electric modulus and M'' is imaginary electric modulus. The variations in these parameters M' and M'' for all composition as a function of frequency is shown in Figure 15(a) and Figure 15(b). The variation in M' and M'' peaks is found due to the occurrence of relaxation phenomenon (frequency dependent variation in conductivity) (J. K. Khan et al., 2020). The function of the conductive grain and low conducting grain boundaries shifts as the strength of the applied field changes, which increase of Fe^{2+} and Fe^{3+} hopping. As a result, it is critical to understand the conduction process, whether it is caused by the grain or the grain boundary.

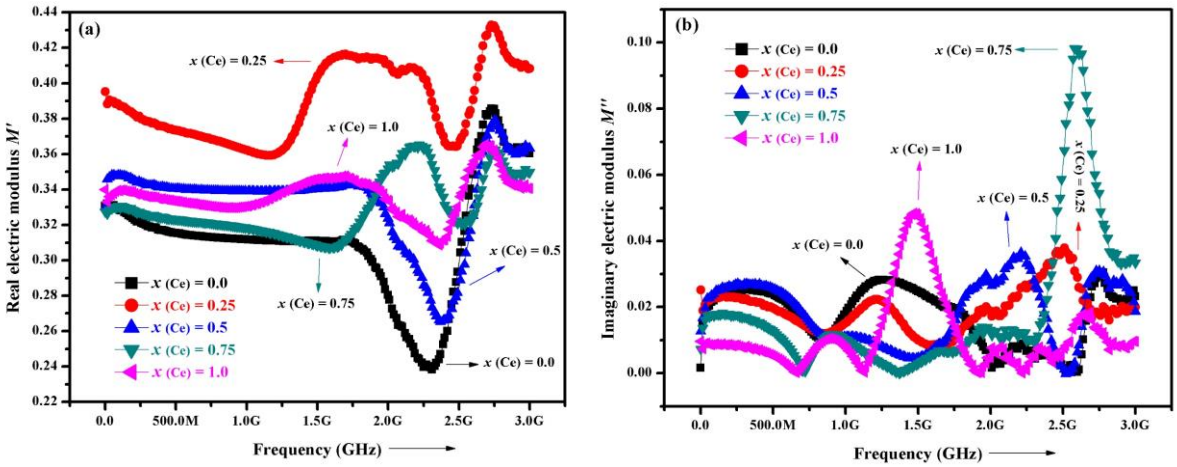

Figure 15: (a) Variation in real electric modulus as a function of frequency (b) Variation in imaginary electric modulus as a function of frequency

The magnitude of real modulus is high at low frequencies and is constant up to between 1.5 – 2 GHz. After 2 GHz it gradually decreases in dispersion with increasing frequency till to 2.5 GHz, except at (x = 0.25), where it increases to its highest value at 1 GHz. In the conduction mechanism, this reflects charge carrier mobility over a limited distance, which related to a loss of restoring power and responsible for charge carrier mobility in the occurrence of an induced electric field. This property specifies that electrode polarization has a negligible effect on the material, (Costa, Pires Jr, Terezo, Graca, & Sombra, 2011) which are not much applied on (x = 0.25). The values of real and imaginary electric modulus from 1 MHz – 3 GHz are given in the (Table 6).

Table 6
Measured values of Real (Z′) and imaginary (Z″), Real (M′) and imaginary (M″) of cerium substituted barium hexaferrites $BaCe_xFe_{12-x}O_{19}$ nanoparticles at (x = 0.0, 0.25, 0.5, 0.75, and 1.0) in the frequency range of 1 MHz – 3 GHz

Parameters	Frequency	x = 0.0	x = 0.25	x = 0.5	x = 0.75	x = 1.0
	1 MHz	384	6000	3010	1740	2290
	1 GHZ	4.44	3.66	2.62	2.36	1.78
Z′ (Ω)	2.5 GHz	0.145	3.6	0.109	6.39	0.708
	3 GHz	1.84	1.58	1.48	2.65	0.76
	1 MHz	78700	94000	78500	77900	80900
	1 GHz	73.7	85.6	75.3	78.2	0.03
Z″ (Ω)	2.5 GHz	28.9	34.9	27.4	30.5	31.9
	3 GHz	28.6	32.4	28.8	27.7	27
	1 MHz	0.33	0.39	0.33	0.33	0.34
	1 GHZ	0.311	0.362	0.331	0.312	0.33
M′	2.5 GHz	0.31	0.37	0.29	0.32	0.34
	3 GHz	0.36	0.4	0.37	0.35	0.34
	1 MHz	0.0012	0.023	0.013	0.0073	0.0097
	1 GHz	0.012	0.012	0.012	0.0099	0.0075
M″	2.5 GHz	0.0015	0.032	0.0011	0.062	0.0074
	3 GHz	0.023	0.012	0.012	0.033	0.0091

4. Conclusions

The cerium (Ce^{+3}) substituted barium hexaferrite ($BaCe_xFe_{12-x}O_{19}$) nanoparticles were successfully synthesized with various Ce^{+3} concentrations (x = 0.0, 0.25, 0.5, 0.75, and 1.0) by using the sol-gel auto combustion method and were investigated by various techniques such as XRD, FTIR and dielectric measurements in order to determine their structural, internal and electric properties. The formation of Ce^{3+} substituted $BaCe_xFe_{12-x}O_{19}$ and the hexagonal structure has been confirmed with the help of XRD patterns by using Rietveld refinement. The refined patterns show that at 2θ = 32°, very extreme peaks with (107) *hkl* formed, which is found to be the perfect peak for hexaferrite nanoparticles. No impurity phase is detected. The measured grain size for each sample has shown correlations with XRD results, indicating that the prepared samples are crystalline. Crystalline size is calculated by Debye Scherrer method, W–H method and SSP method. The smallest crystalline size is found 16 nm by Debye Scherrer Equation. Lattice constant a is

found to decrease, due to the octahedral site replacing a broad radius of Ce^{3+} ion (1.034) with a smaller radius of Fe^{3+} ion (0.64), while lattice constant *c* found increases. Fourier transform infrared spectroscopy (FTIR) studies shows the structural changes and chemical effects. The IR-Spectra of $BaCe_xFe_{12-x}O_{19}$ with different Ce^{+3} concentrations, the two stretching bands tetrahedral and octahedral sites were observed between 400 – 620 cm^{-1}, which exhibited the characteristic features of hexagonal structure, confirming the formation of Hexaferrite nano particles. The dielectric studies are carried out in a frequency range from 1 MHz – 3 GHz, following the Maxwell Wagner model. The AC conductivity of all the samples is low at low frequency range. However, in the high frequency range it exhibits dispersive behavior which shows the conductivity improves. Such behavior is due to the grain effect at high frequency. The real and imaginary impedance were high at low frequency, as soon frequency increases impedance decreases to the lowest value and shows constant behavior, which is attributed to the release of space charges. The real and imaginary modulus analysis conducted to the understand of the grain and grain boundary effect. The variation in M' and M'' is due to the occurrence of relaxation phenomenon. These dielectric properties can be utilized in high frequency devices, microwave technologies, high storage devices, and semiconductor devices.

Acknowledgements

We appreciate the assistance, funds, and facilities provided by the ORIC of Baluchistan University of Information Technology, Engineering, and Management Sciences (BUITEMS), Quetta, Pakistan, University of Karachi, Sindh, Pakistan, and the Institute of Physics, The Islamia University of Bahawalpur, Punjab, Pakistan, in completing this research work in the department of physics.

References

Al-Hilli, M. F., Li, S., & Kassim, K. S. (2009). Microstructure, electrical properties and Hall coefficient of europium-doped Li–Ni ferrites. *Materials Science and Engineering: B, 158*(1-3), 1-6.

Al-Hilli, M. F., Li, S., & Kassim, K. S. (2012). Structural analysis, magnetic and electrical properties of samarium substituted lithium–nickel mixed ferrites. *Journal of Magnetism and Magnetic Materials, 324*(5), 873-879.

Biju, V., Sugathan, N., Vrinda, V., & Salini, S. (2008). Estimation of lattice strain in nanocrystalline silver from X-ray diffraction line broadening. *Journal of materials science, 43*(4), 1175-1179.

Bindu, P., & Thomas, S. (2014). Estimation of lattice strain in ZnO nanoparticles: X-ray peak profile analysis. *Journal of Theoretical and Applied Physics, 8*(4), 123-134.

Brightlin, B., & Balamurugan, S. (2016). The effect of post annealing treatment on the citrate sol–gel derived nanocrystalline BaFe 12 O 19 powder: Structural, morphological, optical and magnetic properties. *Applied Nanoscience, 6*(8), 1199-1210.

Chandrasekaran, G., Selvanandan, S., & Manivannane, K. (2004). Electrical and FTIR studies on Al substituted Mn–Zn mixed ferrites. *Journal of Materials Science: Materials in Electronics, 15*(1), 15-18.

Chang, S., Kangning, S., & Pengfei, C. (2012). Microwave absorption properties of Ce-substituted M-type barium ferrite. *Journal of Magnetism and Magnetic Materials, 324*(5), 802-805.

Choopani, S., Keyhan, N., Ghasemi, A., Sharbati, A., & Alam, R. S. (2009). Structural, magnetic and microwave absorption characteristics of BaCoxMnxTi2xFe12− 4xO19. *Materials Chemistry and Physics, 113*(2-3), 717-720.

Costa, M., Pires Jr, G., Terezo, A., Graca, M., & Sombra, A. (2011). Impedance and modulus studies of magnetic ceramic oxide Ba2Co2Fe12O22 (Co2Y) doped with Bi2O3. *Journal of Applied Physics, 110*(3), 034107.

Farid, M. T., Ahmad, I., Murtaza, G., Ali, I., & Ahmad, I. (2016). Structural, Electrical and Dielectric Behavior of Ni x Co 1-x Pr y Fe 2-y O 4 Nano-Ferrites Synthesized by Sol-Gel Method. *Journal of the Chemical Society of Pakistan, 38*(6).

Gilani, Z. A., Warsi, M. F., Anjum, M. N., Shakir, I., Naseem, S., Riaz, S., & Khan, M. A. (2015). Structural and electromagnetic behavior evaluation of Nd-doped lithium–

cobalt nanocrystals for recording media applications. *Journal of alloys and compounds, 639*, 268-273.
Gilani, Z. A., Warsi, M. F., Khan, M. A., Shakir, I., Shahid, M., & Anjum, M. N. (2015). Impacts of neodymium on structural, spectral and dielectric properties of LiNi0. 5Fe2O4 nanocrystalline ferrites fabricated via micro-emulsion technique. *Physica E: Low-dimensional Systems and Nanostructures, 73*, 169-174.
Hussain, S., Shah, N. A., Maqsood, A., Ali, A., Naeem, M., & Syed, W. A. A. (2011). Characterization of Pb-doped Sr-ferrites at room temperature. *Journal of superconductivity and novel magnetism, 24*(4), 1245-1248.
Iqbal, M. J., Ashiq, M. N., Hernández-Gómez, P., Muñoz, J. M. M., & Cabrera, C. T. (2010). Influence of annealing temperature and doping rate on the magnetic properties of Zr–Mn substituted Sr-hexaferrite nanoparticles. *Journal of alloys and compounds, 500*(1), 113-116.
Jasrotia, R., Singh, V. P., Sharma, R. K., Kumar, P., & Singh, M. (2019). *Analysis of effect of Ag+ ion on microstructure and elemental distribution of strontium W-type hexaferrites.* Paper presented at the AIP Conference Proceedings.
Jasrotia, R., Singh, V. P., Sharma, R. K., & Singh, M. (2019). *Analysis of optical and magnetic study of silver substituted SrW hexagonal ferrites.* Paper presented at the AIP Conference Proceedings.
Jing, J., Liangchao, L., & Feng, X. (2007). Structural analysis and magnetic properties of Gd-doped Li-Ni ferrites prepared using rheological phase reaction method. *Journal of Rare Earths, 25*(1), 79-83.
Joshi, J., Kanchan, D., Joshi, M., Jethva, H., & Parikh, K. (2017). Dielectric relaxation, complex impedance and modulus spectroscopic studies of mix phase rod like cobalt sulfide nanoparticles. *Materials Research Bulletin, 93*, 63-73.
Junaid, M., Khan, M. A., Iqbal, F., Murtaza, G., Akhtar, M. N., Ahmad, M., . . . Warsi, M. F. (2016). Structural, spectral, dielectric and magnetic properties of Tb–Dy doped Li-Ni nano-ferrites synthesized via micro-emulsion route. *Journal of Magnetism and Magnetic Materials, 419*, 338-344.
Karimi, Z., Mohammadifar, Y., Shokrollahi, H., Asl, S. K., Yousefi, G., & Karimi, L. (2014). Magnetic and structural properties of nano sized Dy-doped cobalt ferrite synthesized by co-precipitation. *Journal of Magnetism and Magnetic Materials, 361*, 150-156.
Khan, J. K., Khalid, M., Chandio, A. D., Shahzadi, K., Uddin, Z., Mustafa, G., . . . Gilani, Z. A. (2020). Properties of Al 3+ substituted nickel ferrite (NiAl x Fe 2-x O 4) nanoparticles synthesised using wet sol-gel auto-combustion. *Journal of Sol-Gel Science and Technology*, 1-12.
Khan, M. A., Sabir, M., Mahmood, A., Asghar, M., Mahmood, K., Khan, M. A., . . . Warsi, M. F. (2014). High frequency dielectric response and magnetic studies of Zn1− xTbxFe2O4 nanocrystalline ferrites synthesized via micro-emulsion technique. *Journal of Magnetism and Magnetic Materials, 360*, 188-192.
Kumar, R., & Kar, M. (2016). Lattice strain induced magnetism in substituted nanocrystalline cobalt ferrite. *Journal of Magnetism and Magnetic Materials, 416*, 335-341.
Lakhani, V., Pathak, T., Vasoya, N., & Modi, K. (2011). Structural parameters and X-ray Debye temperature determination study on copper-ferrite-aluminates. *Solid State Sciences, 13*(3), 539-547.
Li, C.-J., Wang, B., & Wang, J.-N. (2012). Magnetic and microwave absorbing properties of electrospun Ba (1− x) LaxFe12O19 nanofibers. *Journal of Magnetism and Magnetic Materials, 324*(7), 1305-1311.
Li, L., Chen, K., Liu, H., Tong, G., Qian, H., & Hao, B. (2013). Attractive microwave-absorbing properties of M-BaFe12O19 ferrite. *Journal of alloys and compounds, 557*, 11-17.
Lodhi, M. Y., Mahmood, K., Mahmood, A., Malik, H., Warsi, M. F., Shakir, I., . . . Khan, M. A. (2014). New Mg0. 5CoxZn0. 5− xFe2O4 nano-ferrites: structural elucidation and electromagnetic behavior evaluation. *Current Applied Physics, 14*(5), 716-720.
Manglam, M. K., Kumari, S., Mallick, J., & Kar, M. (2021). Crystal structure and magnetic properties study on barium hexaferrite of different average crystallite size. *Applied Physics A, 127*(2), 1-12.
Martirosyan, K., Galstyan, E., Hossain, S., Wang, Y.-J., & Litvinov, D. (2011). Barium hexaferrite nanoparticles: synthesis and magnetic properties. *Materials Science and Engineering: B, 176*(1), 8-13.

Mozaffari, M., Amighian, J., & Darsheshdar, E. (2014). Magnetic and structural studies of nickel-substituted cobalt ferrite nanoparticles, synthesized by the sol–gel method. *Journal of Magnetism and Magnetic Materials, 350*, 19-22.

Muneer, I., Farrukh, M. A., & Raza, R. (2020). Influence of annealing temperature on the physical and photoelectric properties of Gd/Fe 1.727 Sn 0.205 O 3 nanoparticles for solid oxides fuel cell application. *Journal of Sol-Gel Science and Technology, 94*(1), 98-108.

Raju, P., & Murthy, S. (2013). Microwave-hydrothermal synthesis of CoFe2O4-TiO2 nanocomposites. *Advanced materials letters, 4*(1), 99-105.

Reddy, C. V., Babu, B., Reddy, I. N., & Shim, J. (2018). Synthesis and characterization of pure tetragonal ZrO2 nanoparticles with enhanced photocatalytic activity. *Ceramics International, 44*(6), 6940-6948. doi:https://doi.org/10.1016/j.ceramint.2018.01.123

Redinz, J. A. (2011). Forces and work on a wire in a magnetic field. *American Journal of Physics, 79*(7), 774-776.

Şelte, A., & Özkal, B. (2019). Crystallite size and strain calculations of hard particle reinforced composite powders (Cu/Ni/Fe-WC) synthesized via mechanical alloying. *Proceedings of the Estonian Academy of Sciences, 68*(1).

Sheikh, F. A., Khalid, M., Shifa, M. S., Aslam, S., Perveen, A., ur Rehman, J., . . . Gilani, Z. A. (2019). Effects of bismuth on structural and dielectric properties of cobalt-cadmium spinel ferrites fabricated via micro-emulsion route. *Chinese Physics B, 28*(8), 088701.

Singh, N., Agarwal, A., Sanghi, S., & Singh, P. (2011). Synthesis, microstructure, dielectric and magnetic properties of Cu substituted Ni–Li ferrites. *Journal of Magnetism and Magnetic Materials, 323*(5), 486-492.

Singh, P., Babbar, V., Razdan, A., Srivastava, S., Agrawal, V., & Goel, T. (2006). Dielectric constant, magnetic permeability and microwave absorption studies of hot-pressed Ba-CoTi hexaferrite composites in X-band. *Journal of materials science, 41*(21), 7190-7196.

Tatarchuk, T., Bououdina, M., Macyk, W., Shyichuk, O., Paliychuk, N., Yaremiy, I., . . . Pacia, M. (2017). Structural, optical, and magnetic properties of Zn-doped CoFe 2 O 4 nanoparticles. *Nanoscale research letters, 12*(1), 1-11.

Tatarchuk, T., Bououdina, M., Paliychuk, N., Yaremiy, I., & Moklyak, V. (2017). Structural characterization and antistructure modeling of cobalt-substituted zinc ferrites. *Journal of alloys and compounds, 694*, 777-791.

Tatarchuk, T., Myslin, M., Mironyuk, I., Bououdina, M., Pędziwiatr, A. T., Gargula, R., . . . Kurzydło, P. (2020). Synthesis, morphology, crystallite size and adsorption properties of nanostructured Mg–Zn ferrites with enhanced porous structure. *Journal of alloys and compounds, 819*, 152945.

Wang, L., & Hu, H. (2005). Flexural wave propagation in single-walled carbon nanotubes. *Physical Review B, 71*(19), 195412.

Zak, A. K., Majid, W. A., Abrishami, M. E., & Yousefi, R. (2011). X-ray analysis of ZnO nanoparticles by Williamson–Hall and size–strain plot methods. *Solid State Sciences, 13*(1), 251-256.